

# Hybrid Graphene Ribbon/Carbon Electrodes for High-Performance Energy Storage

Anna K. Farquhar, Mustafa Supur, Scott R. Smith, Colin Van Dyck, and Richard L. McCreery\*

The utility of supercapacitors for both fixed and portable energy storage would be greatly enhanced if their energy density could be increased while maintaining their high power density, fast charging time, and low cost. This study describes a simple, solution-phase, scalable modification of carbon materials by a covalently bonded “brush” of hydrogen-terminated graphene ribbons (GRs) with layer thicknesses of 2–20 nm, resulting in a 20–100 times increase in the areal capacitance of the unmodified electrode surface. On a flat  $sp^2$  carbon surface modified by GRs, the capacitance exceeds  $1200 \mu\text{F cm}^{-2}$  in  $0.1 \text{ M H}_2\text{SO}_4$  due to a distinct type of pseudocapacitance during constant current charge/discharge cycling. Modification of high surface area carbon black electrodes with GRs yields capacitances of  $950\text{--}1890 \text{ F g}^{-1}$ , power densities  $>40 \text{ W g}^{-1}$ , and minimal change in capacitance during 1500 charge/discharge cycles at  $20 \text{ A g}^{-1}$ . A capacitance of  $1890 \text{ F g}^{-1}$  affords an energy density of  $318 \text{ Wh kg}^{-1}$  operating at  $1.1 \text{ V}$  and  $590 \text{ Wh kg}^{-1}$  at  $1.5 \text{ V}$ . The projected energy density of a hybrid GR/carbon supercapacitor greatly exceeds the current  $10 \text{ Wh kg}^{-1}$  for commercial supercapacitors and approaches that of lithium ion batteries.

available carbon-based supercapacitors are in the range of  $100\text{--}150 \text{ F g}^{-1}$  and often use aqueous electrolytes that limit the working voltage to  $<1.2 \text{ V}$ . As a result, the energy storage density of the best commercial supercapacitors is  $\approx 10 \text{ Wh kg}^{-1}$ ,<sup>[2]</sup> compared to  $100\text{--}200 \text{ Wh kg}^{-1}$  for LIBs and  $1000\text{--}2000 \text{ Wh kg}^{-1}$  for gasoline. Graphene and carbon nanotubes have been investigated extensively for SCs,<sup>[3]</sup> as have carbon composites<sup>[4]</sup> and nano-carbon materials.<sup>[5]</sup> While many examples report capacitances of  $200\text{--}500 \text{ F g}^{-1}$  in small-scale investigations,<sup>[3a-c,f,4a,b,6]</sup> they often involve complex or expensive synthetic procedures that are difficult to scale. Activated carbon materials with exceptionally high surface area have attracted much attention for SC applications due to their high double-layer capacitance and low cost compared to other carbon structures.<sup>[3b]</sup> The highly porous structure of these carbon materials responsible for their high capacitance is often difficult to control during

production, and varies greatly across available materials.<sup>[2,3d,7]</sup> Surface modification of these conductive carbon materials with a redox-active molecular layer has been suggested as an alternative to increase their capacitance by introducing a faradaic contribution.<sup>[7,8]</sup> However, deposition of molecular layers on carbon black results in a decrease in double-layer capacitance and porosity, in part by blocking the passage of ions into the pores.<sup>[9]</sup>

In the current study, we report a bottom-up modification method of carbon materials available for SCs by high surface area graphenic components, i.e., graphene ribbons (GRs), to enhance the surface area and charge storage density while maintaining efficient ionic penetration. GRs consist of H-terminated  $sp^2$  hybridized graphene, with fixed width (e.g., 5, 7, ... carbon atoms) and varying lengths from 1 to 20 nm. We modified a conducting carbon substrate surface by two-point C–C covalent bonding between the carbon surface and the GR structures, which enables GRs to act as planar extensions of the carbon electrode. The growth of the graphenic extension can be controlled electrochemically to adjust the thickness of the GR layer on substrate surfaces. In addition to exceptionally high charge storage density, the hybrid GR/carbon electrodes exhibit long cycle life and are made with low-cost materials and procedures that should be readily scalable to high-capacity energy storage applications.

## 1. Introduction

The problem of storing energy from solar, wind, and other renewable energy sources has stimulated major research efforts in batteries and supercapacitors (SCs), particularly for vehicular and portable applications.<sup>[1]</sup> While supercapacitors have higher power density, lower cost, and faster charging time than lithium ion batteries (LIBs), their low energy storage capacity has seriously limited real-world applications. Using the common metric of farad/gram ( $\text{F g}^{-1}$ ), commercially

Dr. A. K. Farquhar, Dr. M. Supur, Dr. S. R. Smith, Prof. R. L. McCreery  
Department of Chemistry  
University of Alberta  
11227 Saskatchewan Drive, Edmonton, Alberta T6G 2G2, Canada  
E-mail: richard.mcCreery@ualberta.ca

Dr. C. Van Dyck, Prof. R. L. McCreery  
Nanotechnology Research Centre  
National Research Council Canada  
11421 Saskatchewan Drive, Edmonton, Alberta T6G 2M9, Canada

 The ORCID identification number(s) for the author(s) of this article can be found under <https://doi.org/10.1002/aenm.201802439>.

DOI: 10.1002/aenm.201802439

## 2. Results and Discussion

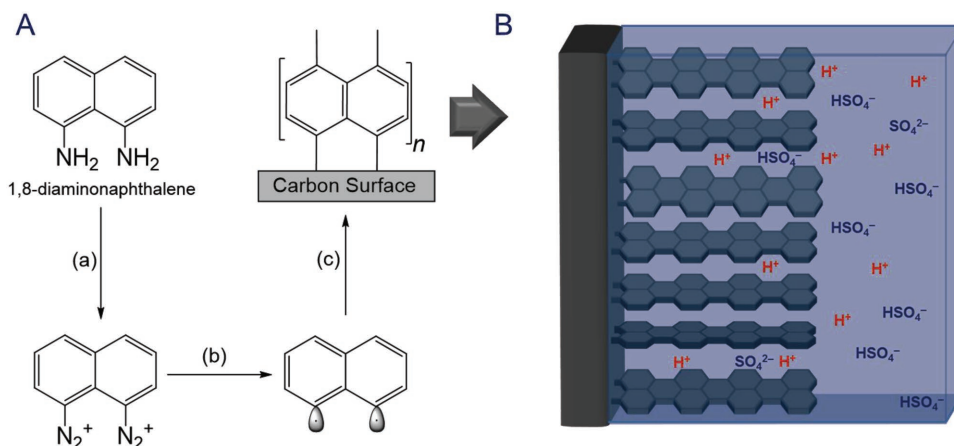
The growth of graphenic extensions on carbon substrates was achieved by electrochemical reduction of aryl diazonium reagents in solution. Grafting was initiated by covalent anchoring of a 1,8-naphthalene biradical derived from its diazonium precursor, as shown in **Scheme 1**. Successive biradical formation maintains the growth of rylene-type GRs, resulting in a layer of rigid, hydrogen-terminated structures with adjustable thickness<sup>[10]</sup> and coverage comparable to that of other diazonium-derived surface layers on carbon ( $\approx 4 \times 10^{-10}$  mol cm<sup>-2</sup>).<sup>[11]</sup> Additional biradical formation continues GR growth, resulting in a “brush” of GRs bonded to the electrode, with individual ribbons presumably having random rotations across the surface. Extensive characterization of the GR layer on flat carbon surfaces by Raman and UV-vis absorption spectroscopy, and electronic conduction was reported previously.<sup>[10]</sup> The covalently bonded GR layer is highly conductive due to strong electronic coupling with the electrode via two-point binding as well as extensive conjugation into the planar ribbon resulting from the double diazonium synthesis. To examine their electrochemical capacitance, GRs were formed initially on pyrolyzed photoresist films (PPF), which is a very flat (<0.5 rms roughness by atomic force microscopy [AFM]), sp<sup>2</sup> hybridized carbon material with low electrochemical capacitance.<sup>[12]</sup>

Modification of carbon surfaces<sup>[13]</sup> and PPF<sup>[14]</sup> with single diazonium reagents yielding single-point binding has been studied extensively with applications in both electrochemistry and molecular electronics.<sup>[15]</sup> We first examined the molecular layer obtained by the reduction of 1-diazonium naphthalene, which can only form one-point bonding to the carbon surface and between naphthalene units, in order for comparison to two-point binding via **Scheme 1**. Voltammetry of unmodified PPF in 0.1 M H<sub>2</sub>SO<sub>4</sub> shows a typical double-layer capacitive response of  $\approx 30$   $\mu\text{F cm}^{-2}$  (**Figure 1A**). Reduction of 1-diazonium naphthalene yields a covalently bonded film of singly bonded naphthalene oligomers with a thickness of 4.5 nm determined by AFM (as described in **Figure S1** in the Supporting Information). The

double-layer capacitance decreased significantly to  $\approx 6$   $\mu\text{F cm}^{-2}$ , as expected for a typical organic film on the electrode surface (**Figure 1A**). The same procedure with the double diazonium reagent shown in **Scheme 1** produces a 12.3 nm thick organic film with the dramatically different voltammetric results of **Figure 1B**.

The PPF/GR electrode under identical conditions to PPF alone exhibits much higher capacitance as well as an apparent redox feature at  $\approx 0.2$  V versus Ag/AgCl (voltammograms vs scan rate for PPF and PPF/GR are provided in **Figure S3** in the Supporting Information). Plots of current versus scan rate at several potentials are linear (**Figure S4**, Supporting Information), with slopes indicating a capacitance of 26.9  $\mu\text{F cm}^{-2}$  at  $E = +0.2$  V for PPF and 1860  $\mu\text{F cm}^{-2}$  for PPF/GR at the same potential. **Figure 1C** at slower scan rates shows structure in the 0.0 to +0.4 V potential region, and neither these nor the large peaks in **Figure 1B** were ever observed for unmodified PPF. **Figure 1D** extends the voltammetric scan range to the solvent breakdown limits in both 0.1 M H<sub>2</sub>SO<sub>4</sub> and 0.1 M NaCl, showing that the enhanced GR capacitance extends over a broad potential range with significantly more negative potentials accessible than on bare PPF. The voltammetric results clearly indicate three features of the GR modification relevant to supercapacitors: an increase of areal capacitance by a factor of 20–70, “pseudocapacitance” from several redox events in the potential range of +0.5 to –0.6 V, and extension of the useful potential range from  $\approx 1.4$  V for PPF to  $\approx 2.0$  V in H<sub>2</sub>SO<sub>4</sub> and  $\approx 2.5$  V in NaCl electrolyte.

The capacitance over the entire –0.2 to +0.8 V potential range was determined using constant current charge/discharge (CD) cycling at 27  $\mu\text{A cm}^{-2}$ , as shown for nine cycles in **Figure 2A,B**. The average stored charge determined during the nine discharge cycles was  $1.238 \pm 0.006$  mC cm<sup>-2</sup> or 1238  $\mu\text{F cm}^{-2}$  for PPF/GR, compared to 23  $\mu\text{F cm}^{-2}$  for unmodified PPF. The significant change in shape between the CD curves of **Figure 2A** and **2B** is likely due to the significant redox contribution to the capacitance apparent in **Figure 1B**. Cycle life was evaluated by performing 10 000 CD cycles at a much higher current density of 1 mA cm<sup>-2</sup>. As shown in **Figure 2C**, there were minor changes in the PPF/GR voltammogram after



**Scheme 1.** A) Surface modification by graphenic ribbons: a) in situ diazotization of amino groups of naphthalene building blocks (1,8-diaminonaphthalene) by *tert*-butyl nitrite (*t*-BuNO<sub>2</sub>) in Ar-bubbled acetonitrile at room temperature, b) electroreduction of diazonium ions yielding aryl biradical and N<sub>2</sub>, and c) successive grafting of generated naphthalene biradicals on the conducting carbon surface and to already grafted naphthalene units, yielding a GR-modified carbon surface. B) Illustration of hybrid GR/carbon electrode with aqueous H<sub>2</sub>SO<sub>4</sub> electrolyte. Illustration is adapted with permission.<sup>[10]</sup> Copyright 2018, American Chemical Society.

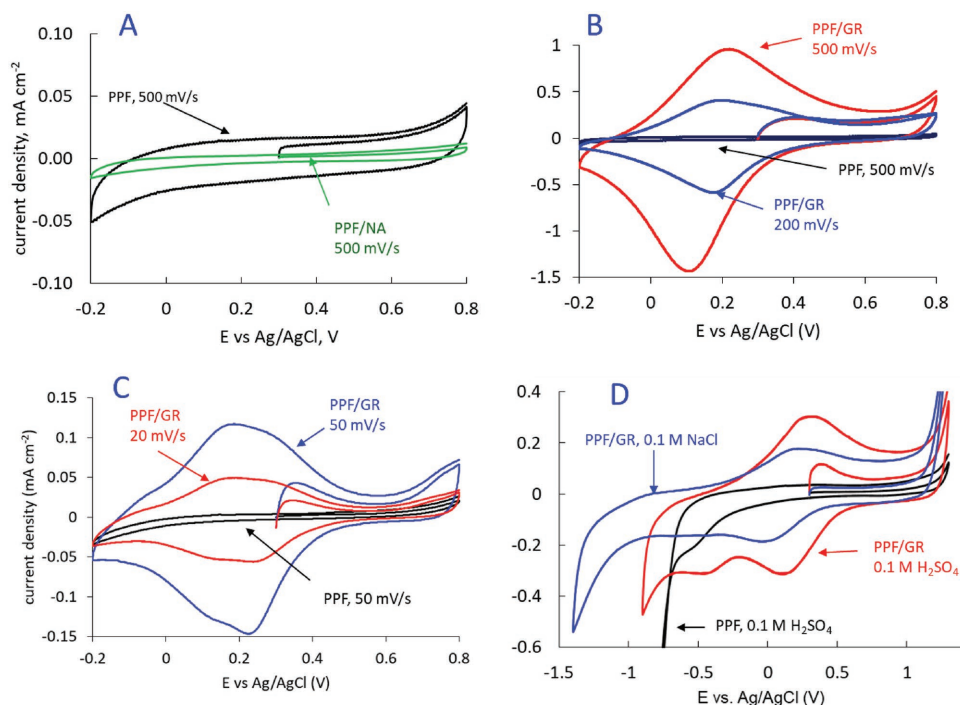


**Figure 1.** Electrochemistry of flat carbon electrodes (PPF) in 0.1 M H<sub>2</sub>SO<sub>4</sub> before and after surface modification. A) Voltammetry of PPF and PPF with singly bonded naphthalene oligomers at 500 mV s<sup>-1</sup>, as indicated. B) Voltammetry of PPF and PPF/GR at 200 and 500 mV s<sup>-1</sup>, as indicated. C) PPF/GR in 0.1 M H<sub>2</sub>SO<sub>4</sub> at 20 and 50 mV s<sup>-1</sup>, compared to bare PPF at 50 mV s<sup>-1</sup>. D) Voltammetry comparison in H<sub>2</sub>SO<sub>4</sub> and NaCl, 100 mV s<sup>-1</sup>. Voltammetry was initiated at the open-circuit potential of +0.3 V in all cases.

10 000 cycles, during which the capacitance decreased by ≈25% (Figure S7, Supporting Information). For unmodified PPF at 0.1 mA cm<sup>-2</sup>, the capacitance increased by a factor of 3 after

10 000 cycles (Figure S7, Supporting Information), with the onset and growth of redox features at +0.25 and +0.55 V versus Ag/AgCl (Figure 2D). The origin of the capacitance decrease for

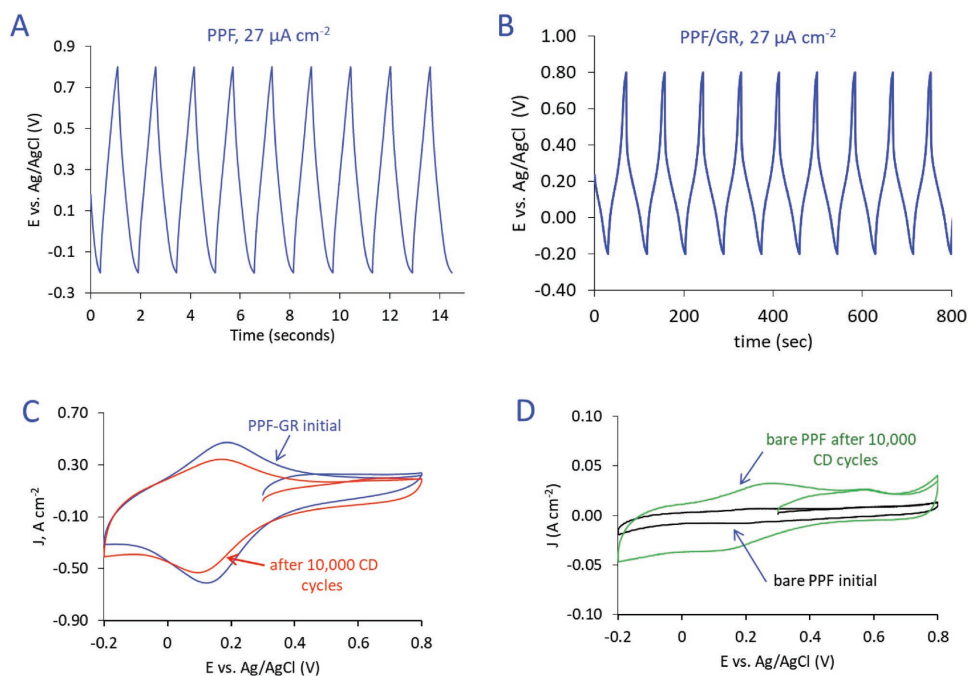


**Figure 2.** A) Charge/discharge cycles for unmodified PPF in 0.1 M H<sub>2</sub>SO<sub>4</sub> with a constant current of 27 μA cm<sup>-2</sup> and potential range of -0.2 to +0.8 V. B) Same procedure for PPF with 12.3 nm GR film; note very different time scale. C) Voltammetry at 200 mV s<sup>-1</sup> for PPF/GR before and after 10 000 CD cycles at 1 mA cm<sup>-2</sup>. D) Same for unmodified PPF cycled at 0.1 mA cm<sup>-2</sup>.

the flat PPF/GR electrode is not clear, but it was not observed with the high surface area, GR-modified carbon electrodes described below.

An initial consideration of the origin of enhanced capacitance by GR modification is the increase in microscopic surface area provided by the graphene ribbon layer. Assuming the GR coverage is  $\approx 4 \times 10^{-10}$  mol cm<sup>-2</sup> and an arbitrary average tilt angle of 45°, the length of each ribbon is 17.4 nm, and that one side of every GR is accessible to the electrolyte,<sup>[16]</sup> the microscopic area would increase by a factor of 30 compared to the flat surface based solely on geometry. The observed capacitance of 1238  $\mu\text{F cm}^{-2}$  corresponds to 41  $\mu\text{F cm}^{-2}$  of microscopic area, and this estimate would increase if the ribbons were not fully accessible to the electrolyte. Examples of microscopic capacitance reported for supercapacitors include 22  $\mu\text{F cm}^{-2}$  for activated carbon,<sup>[17]</sup> 25  $\mu\text{F cm}^{-2}$  for oxidized graphene,<sup>[18]</sup> and 38–49  $\mu\text{F cm}^{-2}$  for carbon composites,<sup>[19]</sup> so a microscopic capacitance of 41  $\mu\text{F cm}^{-2}$  for the current graphene ribbons is within the range reported in the literature. However, this analysis also yields the surprising prediction that 32 electrons are injected into each GR, and that the GR can be polarized and charged as if it were metallic. A practical consequence of this result is the dominance of the GR capacitance relative to the substrate carbon, which is likely to significantly affect the choice of surface area and pore size of substrate materials.

The metallic character of chemisorbed GRs with widths of 0.7 nm and lengths of 2–20 nm implied by the experimental results was examined theoretically by a density functional theory (DFT)-based simulation with periodic boundary conditions of a model system shown in **Figure 3**. GRs are anchored to an infinite and periodic graphite surface, assuming two covalent C–C

bonds on the graphite edge plane (Figure 3A).<sup>[10]</sup> The surface coverage is 66 Å<sup>2</sup> per ribbon ( $2.5 \times 10^{-10}$  mol cm<sup>-2</sup>). After geometry optimization, an implicit water solvent (dielectric constant = 80) was introduced between and beyond the outer edge of the ribbons. Green's function formalism<sup>[20]</sup> was used to apply a potential of +5 V at the outer GR edge. The resulting electrostatic potential through the graphite/GR/water system is reported as a contour plot in Figure 3B for a 4 nm long GR, viewed from the long edge of the ribbon relative to the graphite electrode, simulated as an infinite charged plate at the top of the ribbon. The red region has the same potential as the graphite, clearly indicating that the metallic character of the graphite electrode extends *inside* the ribbon, with progressive confinement and loss of the metallic character as the end of the ribbon is reached.

The metallicity of the ribbon is a consequence of the direct and strong coupling to the carbon substrate, while the confinement effect is induced by the dielectric solvent, as described in Section 9 in the Supporting Information. Increasing the GR length to 20 nm and 46 naphthalene subunits (Figure 3C) shows that the confinement region remains localized at the edge of the ribbon and metallic character extends  $\approx 18$  nm from the graphite surface. This theoretical characterization confirms that the two-point covalent bonding between the GR and the graphite edge results in extended metallic character of the electrode into a dielectric medium for at least  $\approx 18$  nm, effectively producing a highly porous carbon electrode. Ion penetration between adjacent ribbons is certainly possible, with accompanying compensation of charge injected into the GR from the electrode. However, the areal capacitance of single-layer graphene is reportedly limited to 10  $\mu\text{F cm}^{-2}$ , with a low density of states (DOS) near the Fermi energy.<sup>[21]</sup> Assuming GRs have a similar DOS, we estimate that the capacitance would saturate at 8 electrons per volt into each ribbon, not 32 as observed experimentally. Several possibilities that would enhance the GR capacity include a higher DOS than graphene due to finite ribbon width, increased DOS due to bending and deformation of the ribbon,<sup>[21,22]</sup> oxidation of the ribbon to generate redox-active functional groups,<sup>[23]</sup> and structural defects derived from the radical-mediated diazonium surface modification. Preliminary X-ray photoelectron spectroscopy results indicated a nitrogen content in the GR-modified electrodes of 6–12 atom%, depending on formation conditions. This nitrogen may be present in aminophenyl structures or azo linkages,<sup>[24]</sup> which may be redox active. Redox centers would explain the large pseudocapacitance of PPF/GR, and we estimate that one 2-electron center every three naphthalene subunits would correspond to 32 electrons stored in a 17.4 nm long ribbon.

Structural changes in PPF/GR electrodes during charging and possible redox processes were investigated experimentally with in situ UV–vis absorption and Raman spectroscopy. PPF can be made sufficiently thin ( $\approx 50$  nm) to provide partial optical transparency, such that optical absorbance measurements can be conducted in situ using the beam of a conventional UV–vis spectrometer at normal incidence to the PPF surface.<sup>[25]</sup> The black curve of **Figure 4A** is the absorbance of PPF on quartz in 0.1 M H<sub>2</sub>SO<sub>4</sub>, with a path length in solution of 1.0 cm, relative to the cell, blank quartz, and electrolyte (see Section 6 in the Supporting Information for details). The blue curve of **Figure 4A** is a similar PPF electrode after modification

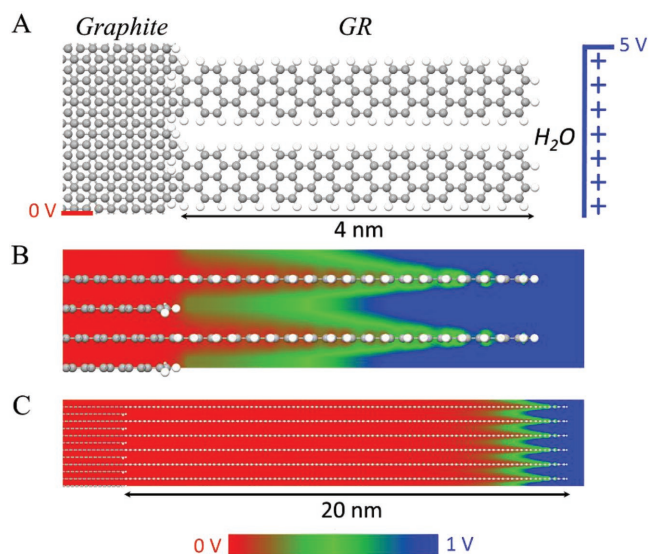


**Figure 3.** A) Structural model of a periodic graphite surface bonded to 4 nm long GRs in water with an applied electrostatic potential of +5 V at the end of the GR. B) Electrostatic potential map of the same structure with the view rotated to observe the long edge of the 4 nm GR. C) Similar plot of potential across a 20 nm long GR. Red color indicates metallic character, with no potential change between the graphite and GR regions. Calculation details are provided in Section 9 in the Supporting Information and ref. [10].

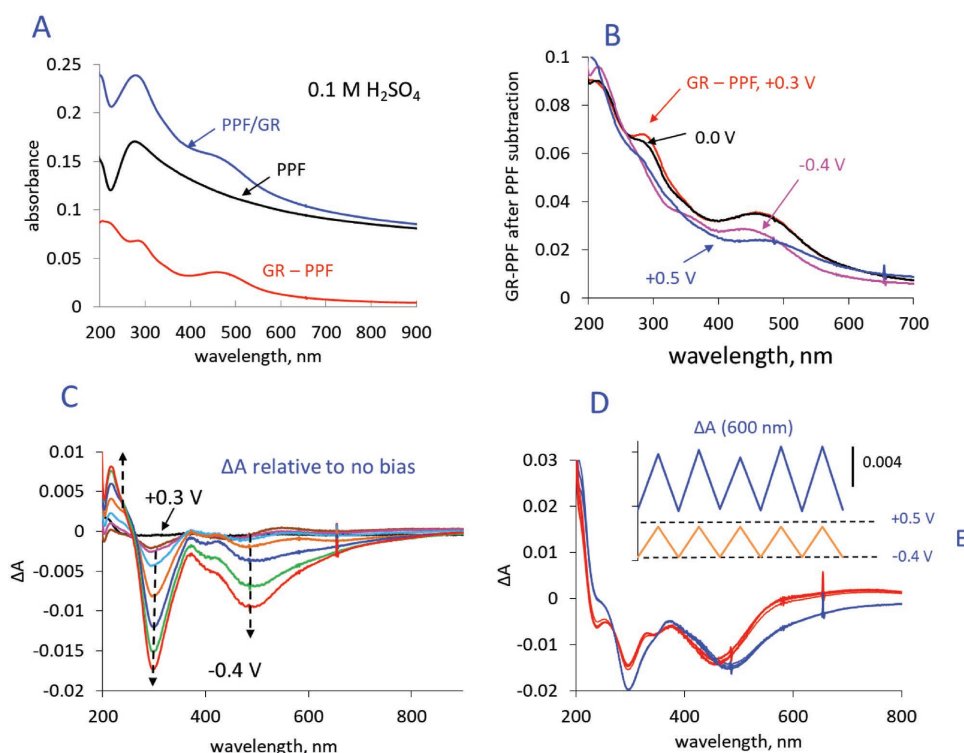


**Figure 4.** UV-vis absorption spectroscopy obtained in transmission geometry of PPF ( $\approx 50$  nm) and PPF/GR ( $\approx 10$  nm) in  $0.1$  M  $\text{H}_2\text{SO}_4$ . A) Unmodified PPF (black), PPF/GR (blue), and PPF/GR after PPF subtraction (red). B) PPF/GR spectra after PPF subtraction with the PPF surface held at the indicated potentials versus Ag/AgCl. C) Change in the PPF-corrected absorbance relative to the initial spectrum without an applied potential. The first spectrum at  $+0.3$  V (black) is flat and the dashed arrows indicate progressive changes as  $E$  decreased to  $-0.4$  V in  $0.1$  V steps. D) Ten spectra obtained after those of panel C, with  $E$  alternated between  $+0.5$  and  $-0.4$  V, as shown in the inset. Spectra are overlays of five spectra for each potential. Except for panel D, all spectra are averages of five spectra acquired successively at a given  $E$ .

with a  $\approx 10$  nm GR film and immersion in  $0.1$  M  $\text{H}_2\text{SO}_4$ , and the red curve is the PPF/GR spectrum after subtraction of the bare PPF spectrum. The absorbance of the GR film is similar to that observed previously in air,<sup>[10]</sup> with broad absorption declining with wavelength, and absorption features at  $\approx 300$  and  $\approx 470$  nm. Absorption peaks for isolated rylenes in solution with structures similar to GRs have been reported previously in the range of  $440$  to  $750$  nm, depending on oligomer length.<sup>[26]</sup> Figure 4B shows spectra for PPF/GR (with PPF absorbance subtracted) obtained in  $0.1$  M  $\text{H}_2\text{SO}_4$  while the electrode potential was controlled by a CHI 660A potentiostat. The spectrum obtained at the approximate open-circuit potential (OCP) of  $+0.3$  V versus Ag/AgCl (red curve) was nearly identical to that before a potential was applied, and is the same curve as that shown in Figure 4A. The black ( $0.0$  V vs Ag/AgCl), pink ( $-0.4$  V), and blue ( $+0.5$  V) curves were obtained at the indicated potentials, and clearly exhibit changes in optical absorption during polarization of the GR relative to the Ag/AgCl reference potential. No such changes were observed for bare PPF under identical conditions (Figure S11, Supporting Information).

While the origins of the UV-vis changes are not readily discernible, there is no question that the electronic structure of the GR is changing with polarization. The course of these effects is more apparent when plotted as the change in absorbance,  $\Delta A$ , relative to the initial spectrum with no bias applied, shown in Figure 4C,D. For Figure 4C, the potential was decreased from

$+0.3$  to  $-0.4$  V in  $0.1$  V steps, resulting in monotonic absorbance losses at  $298$  and  $497$  nm, and an absorbance increase at  $221$  nm. Returning to  $+0.3$  V did not restore the initial spectrum; however, spectra during subsequent excursions to negative and positive potentials were reproducible for at least five cycles. Figure 4D shows four  $\Delta A$  spectra at  $+0.5$  V alternating with four at  $-0.4$  V, using the potential program in the inset. Once the initial changes shown in Figure 4C occurred, the spectra continued to change with applied potential, but could be cycled repeatedly. It is possible that the apparently irreversible changes during the first negative excursion are due to ion and water incursion into the GR brush, which then allows subsequent reversible ion penetration between the ribbons with potential excursions. The absorbance results provide strong evidence for charge injection into the GR, with accompanying changes in electronic structure.

Raman spectroscopy is widely used for characterizing graphene materials, and provides more structural information than UV-vis absorption.<sup>[27]</sup> We recently reported that surface-enhanced Raman spectroscopy (SERS) is useful for characterizing organic film growth on carbon substrates,<sup>[28]</sup> and applied both SERS and unenhanced Raman spectroscopy to monitor PPF/GR electrodes in situ in a cell similar to that used for UV-vis absorption. Figure 5A shows Raman spectra for a GR layer on a Ag film (average thickness =  $10$  nm) on PPF, both in air and in  $0.1$  M  $\text{H}_2\text{SO}_4$ , compared to PPF/GR in air without Ag.

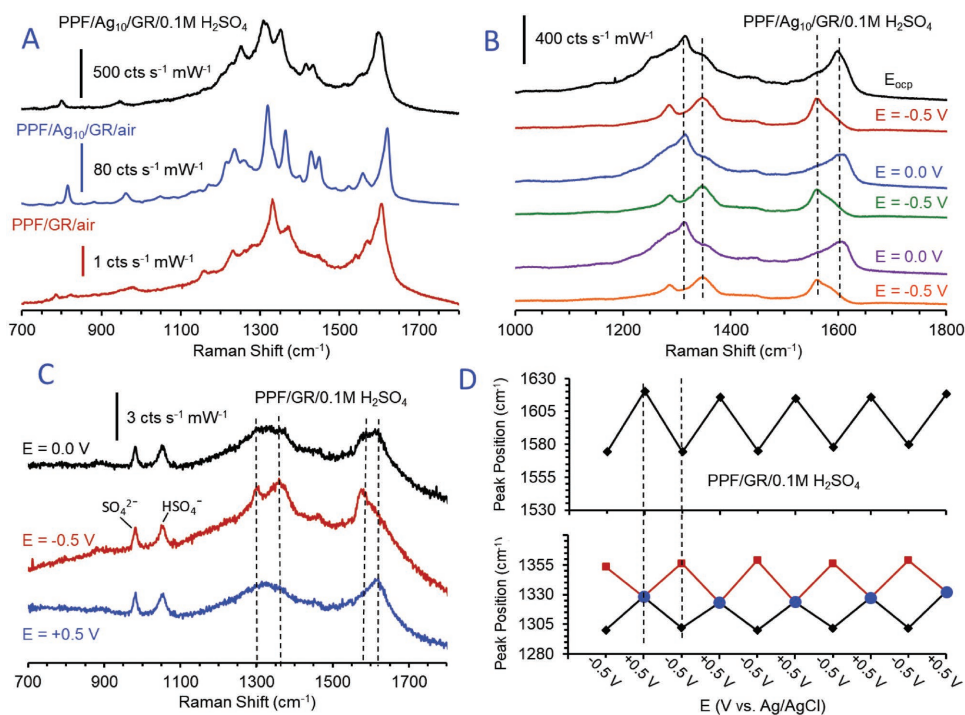


**Figure 5.** Raman spectroscopy with a 532 nm laser of GR films grown on PPF or PPF/Ag (10 nm) as described in Section 7 in the Supporting Information, with a bare PPF spectrum obtained with identical conditions subtracted in all cases. A) Unenhanced (red) in air and enhanced spectra in air (blue) and 0.1 M  $\text{H}_2\text{SO}_4$  (black). B) Enhanced spectra during potential control, with  $E_{\text{OCP}}$  acquired before  $E$  was applied. C) Unenhanced spectra of PPF/GR at indicated potentials, each an average of five spectra. Peaks at  $\approx 980$  and  $1060 \text{ cm}^{-1}$  are due to  $\text{SO}_4^{2-}$  and  $\text{HSO}_4^-$ . D) Positions of unenhanced peaks during alternating  $E$  of  $-0.5$  and  $+0.5 \text{ V}$ , indicating splitting of the  $\approx 1316 \text{ cm}^{-1}$  band.

The peaks in the unenhanced spectrum at  $1609$ ,  $1375$ ,  $1332$ ,  $1235$ , and  $980 \text{ cm}^{-1}$  are very similar to those reported for synthetic nanoribbons based on anthracene (i.e., seven carbon atoms wide).<sup>[29]</sup> The SERS spectra are more intense and better defined than the unenhanced spectra, and all three examples in Figure 5A show major bands at  $\approx 1600$  and  $\approx 1330 \text{ cm}^{-1}$ .<sup>[30]</sup> We previously associated the main GR Raman features with two vibrations predicted by DFT at  $1316$  and  $1612 \text{ cm}^{-1}$  (shown in Figure S13 in the Supporting Information), which are unique to the planar ribbon structure.<sup>[10]</sup> The spectra of Figure 5B were all obtained on the same PPF/GR surface in  $0.1 \text{ M H}_2\text{SO}_4$  at the indicated potentials, starting at the open-circuit potential (top). The significant changes in peak positions with potential clearly indicate changes in bond vibrational energies, which are reversible for at least four cycles between  $0.0$  and  $-0.5 \text{ V}$ . The unenhanced spectra of Figure 5C avoid the problem of Ag oxidation at positive potentials, but also have significantly lower signal/noise ratio than the SERS spectra. The potential was cycled five times in  $0.1 \text{ M H}_2\text{SO}_4$  in the sequence  $-0.5$ ,  $0.0$ ,  $+0.5$ , and  $0.0 \text{ V}$  versus Ag/AgCl, and Figure 5C shows the average of the unenhanced spectra obtained at each potential.

The bands show similar changes with potential to the SERS spectra of Figure 5B, with the  $\approx 1330 \text{ cm}^{-1}$  band splitting when  $E = -0.5 \text{ V}$ . The peak maxima of the  $\approx 1330$  and  $\approx 1620 \text{ cm}^{-1}$  bands during potential cycling are shown in Figure 5D, and confirm that the peak shifts and splittings are reversible and repeatable. Several conclusions about the effect of potential cycling on the PPF/GR structure are available from the Raman results. First, voltammetric current evident in Figure 1 affects

Raman modes associated with the ribbon structure, providing evidence that charge is entering the ribbon rather than some other process. Second, the Raman spectral changes are reversible for at least several cycles, with no additional features evolving over time. Third, both increases and decreases in vibrational frequency with increasing negative potential imply that the high capacitance is due to the ribbon structure itself, rather than some unknown side reaction.

Areal capacitance of a few millifarad per square centimeter observed with flat PPF/GR electrodes may be useful in small-scale applications such as on-chip energy storage,<sup>[3]</sup> but large-scale applications in vehicles and electricity grids require much higher capacity and active surface area. The GR modification was tested on carbon black/steel mesh electrodes prepared using a published procedure<sup>[8]</sup> and Vulcan XCmax22 ( $1360 \text{ m}^2 \text{ g}^{-1}$ ) carbon black from Cabot Corporation. As described in the Experimental Section, electrodes were made by pressing the carbon mixed with polytetrafluoroethylene (PTFE) binder (85/15 w/w) onto a stainless steel mesh, to yield electrodes with areas of  $\approx 0.5 \text{ cm}^2$ , thicknesses of  $150\text{--}200 \mu\text{m}$ , and carbon loading of  $0.53\text{--}0.95 \text{ mg cm}^{-2}$ . Completed electrodes were modified with GR in the same manner as PPF, with adjustments to concentrations and scan parameters provided in the Supporting Information. Figure 6A shows voltammograms ( $2 \text{ mV s}^{-1}$ ) for an XCmax/GR electrode in  $0.1 \text{ M H}_2\text{SO}_4$  before and after GR modification. The large increase in capacitance with GRs is similar to that observed on flat PPF, with the capacitance calculated from the integrated area between  $-0.2$  and  $+0.8 \text{ V}$  increasing from  $159$  to  $1699 \text{ F g}_{\text{CB}}^{-1}$ , with  $\text{g}_{\text{CB}}$  indicating

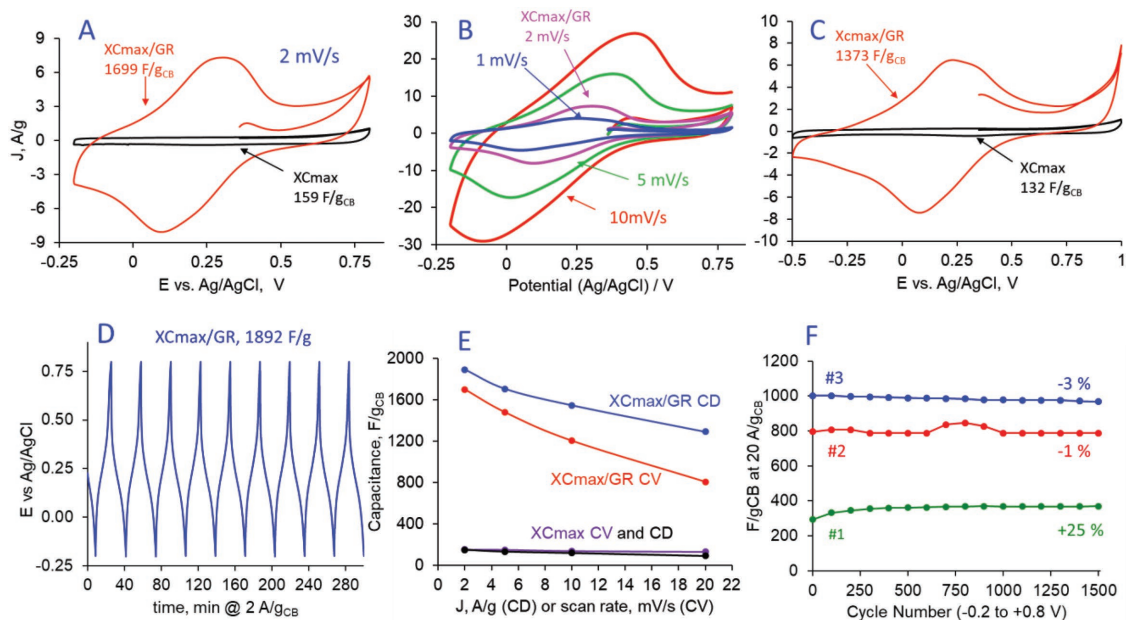


**Figure 6.** Electrochemistry of high surface area XCmax/PTFE composite electrodes in 0.1 M H<sub>2</sub>SO<sub>4</sub>. A) Unmodified (black) and modified (red) voltammograms of XCmax. B) Scan rate dependence over a 1.0 V potential range. C) Voltammetry over a 1.5 V potential range at 2 mV s<sup>-1</sup>. D) Charge/discharge cycles for XCmax/GR at 2 A g<sub>CB</sub><sup>-1</sup> between -0.2 and +0.8 V versus Ag/AgCl. E) Capacitance of XCmax/GR versus CV scan rate (red) and CD current (blue), and for unmodified XCmax. F) Repetitive CD cycles for XCmax/GR at 20 A g<sub>CB</sub><sup>-1</sup>, stated as capacitance versus cycle number. The increase for sample #2 during cycles 700–1000 was due to a temporary interruption in the applied current. Panels A, B, D, and E were obtained on the XCmax/GR sample #2, while panel C used sample #3 (described in Table S5 in the Supporting Information).

the mass of carbon black starting material. Three XCmax/GR electrodes made with the same procedure but with variation in carbon loading yielded capacitances of 945, 1530, and 1699 F g<sub>CB</sub><sup>-1</sup> (mean = 1391 ± 323) by voltammetry at 2 mV s<sup>-1</sup>, and 968, 1680, and 1892 F g<sub>CB</sub><sup>-1</sup> (mean = 1500 ± 413) by CD cycling at 2 A g<sub>CB</sub><sup>-1</sup> (detailed results are provided in Table S5 in the Supporting Information).

The scan rate dependence and peak shape in Figure 6B are consistent with the porous electrode and significant pseudocapacitance contribution from charge injection into the GR. Figure 6C is a voltammogram of XCmax/GR over a +1.0 to -0.5 V range for a different XCmax/GR sample.

The nine CD cycles of Figure 6D at 2 A g<sub>CB</sub><sup>-1</sup> yielded 1886 ± 13 F g<sub>CB</sub><sup>-1</sup> for charging and 1892 ± 2 F g<sub>CB</sub><sup>-1</sup> for discharging, with an average efficiency of 100.3 ± 0.8%. The power density during CD cycles determined by the method of El-Kady et al.<sup>[3c]</sup> ranged from 41 W g<sub>CB</sub><sup>-1</sup> at 2 A g<sub>CB</sub><sup>-1</sup> to 80 W g<sub>CB</sub><sup>-1</sup> at 20 A g<sub>CB</sub><sup>-1</sup>. All three XCmax/GR samples were monitored for 1500 CD cycles at 20 A g<sub>CB</sub><sup>-1</sup> over a period of ≈10 h (each), with the changes in capacitance shown in Figure 6F. As indicated, two samples had minor losses in capacitance after 1500 cycles (-1% and -3%) while the third showed a 25% increase.

The difficulty of scaling laboratory results from F g<sup>-1</sup> of carbon material to large supercapacitors for widespread application is well known,<sup>[3b,31]</sup> often resulting in a factor of 3–4 loss of capacity per unit mass when solvent, electrodes, and packaging are included.<sup>[31]</sup> The 1890 F g<sub>CB</sub><sup>-1</sup> observed for XCmax/GR during charge/discharge cycling is projected to yield energy densities of 318 Wh kg<sup>-1</sup> for operation at 1.1 V and 590 Wh kg<sup>-1</sup> at +1.5 V, with higher values possible if the extended voltage

range observed in Figure 1D is realized in practice. Even with significant losses during scale-up, these estimates greatly exceed the 10 Wh kg<sup>-1</sup> of current commercial supercapacitors, and approach or exceed those currently possible with commercial lithium batteries.

### 3. Conclusions

The results on both flat and high surface area carbon electrodes clearly establish that the GR “brush” electrode has several distinct properties that may be valuable in supercapacitors. First, there is strong electronic coupling between the conducting carbon substrate and the covalently attached GR, which both “extends” the electrode to increase area and permits injection of multiple charges into the GR. Second, the large pseudocapacitance associated with charge injection not only increases capacity but may also be useful in hybrid supercapacitor devices with carbon/GR as one electrode and a metal oxide such as MnO<sub>2</sub> or RuO<sub>2</sub> as the other.<sup>[32]</sup> Third, the fact that the GR itself provides most of the capacitance in the GR brush electrodes (>90%) places quite different requirements on the substrate pore size and surface area, and significant capacity increases may be available with optimization of the substrate and GR deposition conditions. Furthermore, the diazonium-mediated GR modification has several additional practical benefits: (1) GR modification should be useful for a variety of carbon substrates, including flexible materials, microfabricated devices, and carbon nanostructures, in addition to carbon materials used in commercial SCs; (2) hydrogen termination inherent in the GR should extend the useful voltage range and

also be resistant to degradation with prolonged charging and discharging; and (3) production by a solution-phase process, possibly in water,<sup>[8]</sup> from simple chemicals (diamino aromatic precursors and NaNO<sub>2</sub>), requiring no vacuum, high temperatures, or expensive techniques and readily scalable to large quantities.

## 4. Experimental Section

**Fabrication of PPF/GR Substrates:** PPF substrates used in electrochemistry and Raman spectroscopy were prepared using a previously reported procedure.<sup>[12,33]</sup> GRs were grafted to the PPF electrochemically by reduction of 1,8-diazonium naphthalene formed in situ.<sup>[10]</sup> The grafting solution was acetonitrile (15 mL) containing 1,8-diaminonaphthalene ( $2 \times 10^{-3}$  M) and tetrabutylammonium tetrafluoroborate (TBABF<sub>4</sub>, 0.1 M) that was purged for 15 min with argon prior to grafting. *tert*-Butyl nitrite (50  $\mu$ L) was added to convert the diamino precursor into the corresponding aryl diazonium ion. After waiting 2 min to allow diazotization to occur, the PPF chip was submerged in the grafting solution. Electrochemical grafting was performed by a CHI 660A electrochemical workstation via cyclic voltammetry (CV) in a conventional three-electrode cell, with a Pt wire counter electrode and a Ag/Ag<sup>+</sup> (0.01 M AgNO<sub>3</sub> in acetonitrile) reference electrode. The grafting parameters used for cyclic voltammetry are given in the Supporting Information. After grafting the substrates were washed with acetonitrile and dried under nitrogen. For UV-visible spectroscopy, the same grafting procedure was used but the PPF was replaced with optically transparent PPF on Au-framed quartz chips (Figure S8, Supporting Information).

**Fabrication of Vulcan XCmax22/GR Electrodes:** Vulcan XCmax22 carbon black powder was provided by Cabot Corporation. The XCmax22 electrodes were prepared based on a previously reported procedure.<sup>[8]</sup> Carbon black (40 mg) was mixed with polytetrafluoroethylene (7 mg) in a small volume of ethanol to give a homogeneous paste, which was cold-rolled into a film, placed on a circular ( $\approx$ 11 mm diameter) stainless steel grid current collector (80 mesh, 0.127 mm, Alfa Aesar) and pressed for 3 min at  $3 \times 10^7$  Pa. XCmax22 electrodes were modified with GRs using electrochemical deposition from an acetonitrile solution (15 mL) of 1,8-diaminonaphthalene ( $60 \times 10^{-3}$  M) and TBABF<sub>4</sub> (0.1 M) that was purged for 15 min with argon. After purging, the XCmax22 electrodes were immersed in the grafting solution for 30 min to allow the solution to penetrate the porous structure of the electrode while a steady stream of argon was maintained over the solution. During this period, two aliquots of *tert*-butyl nitrite (150  $\mu$ L each) were added to the grafting solution. Cyclic voltammetry was used for grafting, with a Pt wire counter electrode and Ag/Ag<sup>+</sup> (AgNO<sub>3</sub> 0.1 M in acetonitrile) reference electrode. Grafting parameters are given in the Supporting Information. After grafting, electrodes were washed with acetonitrile and dried in air.

**Electrochemical Characterization:** All electrochemical measurements were carried out in a conventional three-electrode cell in 0.1 M H<sub>2</sub>SO<sub>4</sub> that was purged with argon for 10 min prior to measurement. A steady stream of argon was maintained over the solution for the duration of each measurement. A Ag/AgCl (sat. KCl) reference electrode and either a Pt wire (PPF and PPF/GR characterization) or a large area stainless steel mesh (XCmax22 and XCmax22/GR characterization) counter electrode were used. CVs were started at OCP and scanned toward positive potentials first. CVs were recorded in order of increasing scan rate. Constant current charge/discharge measurements were performed by charging electrodes from  $-0.2$  to  $+0.8$  V and then discharging from  $+0.8$  to  $-0.2$  V at an applied current density of 27  $\mu$ A cm<sup>-2</sup> for PPF electrodes and 2 A g<sub>CB</sub><sup>-1</sup> for XCmax22 electrodes. Further experimental details and equations used to calculate capacitance and power density are given in the Supporting Information.

**In Situ UV-Vis and Raman Spectroscopy:** In situ UV-vis spectroscopy was performed on an Agilent 8453 diode array spectrophotometer under bias applied by a CHI 660A electrochemical workstation in a conventional three-electrode arrangement with a Ag/AgCl (sat. KCl)

reference electrode and Pt wire counter electrode in a quartz cell filled with 0.1 M H<sub>2</sub>SO<sub>4</sub> (Figure S9, Supporting Information). In situ Raman spectroscopy measurements utilized the same electrochemical setup as for UV-vis measurements (Figure S12, Supporting Information). The spectrometer was a custom line-focused charge coupled device (CCD) spectrograph,<sup>[34]</sup> with a 38 mm diameter Semrock 532 nm RazorEdge LWP filter. The laser output was filtered with a 12.5 mm diameter Semrock 532 MaxLine laser line filter. The CCD was an Andor Newton-DU970N operated in full vertical binning mode. Further experimental details for both UV-vis and Raman Spectroscopy are given in Sections 6 and 7 in the Supporting Information, respectively.

## Supporting Information

Supporting Information is available from the Wiley Online Library or from the author.

## Acknowledgements

A.K.F. and M.S. contributed equally to this work. This work was supported by the University of Alberta, the National Research Council of Canada, the National Sciences and Engineering Research Council, and Alberta Innovates. The authors acknowledge the computational resources of the Center for Nanoscale Materials (Argonne National Lab), an Office of Science user facility, supported by the U.S. Department of Energy, Office of Science, Office of Basic Energy Sciences, under Contract No. DE-AC02-06CH11357. The authors thank John Marsh at Cabot Corporation for the sample of Vulcan XCmax22 carbon black.

## Conflict of Interest

The authors declare no conflict of interest.

## Keywords

carbon black, diazonium reduction, graphene ribbon, renewable energy, supercapacitors

Received: August 6, 2018

Revised: September 26, 2018

Published online: October 25, 2018

[1] G. Wang, L. Zhang, J. Zhang, *Chem. Soc. Rev.* **2012**, 41, 797.

[2] L. Borchardt, M. Oschatz, S. Kaskel, *Mater. Horiz.* **2014**, 1, 157.

[3] a) Y. Zhu, S. Murali, M. D. Stoller, K. J. Ganesh, W. Cai, P. J. Ferreira, A. Pirkle, R. M. Wallace, K. A. Cychosz, M. Thommes, D. Su, E. A. Stach, R. S. Ruoff, *Science* **2011**, 332, 1537; b) P. Simon, Y. Gogotsi, *Acc. Chem. Res.* **2013**, 46, 1094; c) M. F. El-Kady, V. Strong, S. Dubin, R. B. Kaner, *Science* **2012**, 335, 1326; d) S. T. Bulbula, Y. Lu, Y. Dong, X.-Y. Yang, *New J. Chem.* **2018**, 42, 5634; e) Y. Wang, Z. Shi, Y. Huang, Y. Ma, C. Wang, M. Chen, Y. Chen, *J. Phys. Chem. C* **2009**, 113, 13103; f) Y. Hao, K. Santhakumar, S. P. Amaresh, J. Jae-Hyung, L. Yun Sung, L. Wu, *Nanotechnology* **2017**, 28, 445401.

[4] a) L. G. H. Staaf, P. Lundgren, P. Enoksson, *Nano Energy* **2014**, 9, 128; b) T. Liu, F. Zhang, Y. Song, Y. Li, *J. Mater. Chem. A* **2017**, 5, 17705; c) Y. Yi Han, Z. Lai, Z. Wang, M. Yu, Y. Tong, X. Lu, *Chem. Eur. J.* **2018**, 24, 7312.

- [5] a) H. Wang, Z. Xu, A. Kohandehghan, Z. Li, K. Cui, X. Tan, T. J. Stephenson, C. K. King'ondeu, C. M. B. Holt, B. C. Olsen, J. K. Tak, D. Harfield, A. O. Anyia, D. Mitlin, *ACS Nano* **2013**, *7*, 5131; b) L. Tian, L. Mingxian, Z. Dazhang, G. Lihua, C. Tao, *Adv. Mater.* **2018**, *30*, 1705489.
- [6] a) M. Inagaki, H. Konno, O. Tanaike, *J. Power Sources* **2010**, *195*, 7880; b) J. Pokrzywinski, J. K. Keum, R. E. Ruther, E. C. Self, M. Chi, H. Meyer Iii, K. C. Littrell, D. Aulakh, S. Marble, J. Ding, M. Wriedt, J. Nanda, D. Mitlin, *J. Mater. Chem. A* **2017**, *5*, 13511; c) T. G. Yun, D. Kim, S.-M. Kim, I.-D. Kim, S. Hyun, S. M. Han, *Adv. Energy Mater.* **2018**, *8*, 1800064; d) S. I. Wong, J. Sunarso, B. T. Wong, H. Lin, A. Yuc, B. Jia, *J. Power Sources* **2018**, *396*, 182.
- [7] G. Pognon, T. Brousse, L. Demarconnay, D. Bélanger, *J. Power Sources* **2011**, *196*, 4117.
- [8] G. Pognon, C. Cougnon, D. Mayilukila, D. Bélanger, *ACS Appl. Mater. Interfaces* **2012**, *4*, 3788.
- [9] a) T. Menanteau, C. Benoît, T. Breton, C. Cougnon, *Electrochem. Commun.* **2016**, *63*, 70; b) C. Benoit, D. Demeter, D. Bélanger, C. Cougnon, *Angew. Chem., Int. Ed.* **2016**, *55*, 5318; c) C. Benoit, D. Demeter, D. Bélanger, C. Cougnon, *Angew. Chem.* **2016**, *128*, 5404.
- [10] M. Supur, C. Van Dyck, A. J. Bergren, R. L. McCreery, *ACS Appl. Mater. Interfaces* **2018**, *10*, 6090.
- [11] a) Y.-C. Liu, R. L. McCreery, *J. Am. Chem. Soc.* **1995**, *117*, 11254; b) P. A. Brooksby, A. J. Downard, *Langmuir* **2004**, *20*, 5038.
- [12] S. Ranganathan, R. L. McCreery, *Anal. Chem.* **2001**, *73*, 893.
- [13] D. Belanger, J. Pinson, *Chem. Soc. Rev.* **2011**, *40*, 3995.
- [14] a) F. Anariba, S. H. DuVall, R. L. McCreery, *Anal. Chem.* **2003**, *75*, 3837; b) R. McCreery, J. Wu, R. J. Kalakodimi, *Phys. Chem. Chem. Phys.* **2006**, *8*, 2572; c) S. S. C. Yu, E. S. Q. Tan, R. T. Jane, A. J. Downard, *Langmuir* **2007**, *23*, 4662.
- [15] a) U. M. Tefashe, Q. V. Nguyen, F. Lacroix, J.-C. Lacroix, R. L. McCreery, *J. Am. Chem. Soc.* **2017**, *139*, 7436; b) R. McCreery, H. Yan, A. J. Bergren, *Phys. Chem. Chem. Phys.* **2013**, *15*, 1065; c) A. Bayat, J.-C. Lacroix, R. L. McCreery, *J. Am. Chem. Soc.* **2016**, *138*, 12287; d) H. Yan, A. J. Bergren, R. McCreery, M. L. Della Rocca, P. Martin, P. Lafarge, J. C. Lacroix, *Proc. Natl. Acad. Sci. USA* **2013**, *110*, 5326.
- [16] B. C. Wood, T. Ogitsu, M. Otani, J. Biener, *J. Phys. Chem. C* **2014**, *118*, 4.
- [17] B. Xu, S. Hou, H. Duan, G. Cao, M. Chu, Y. Yang, *J. Power Sources* **2013**, *228*, 193.
- [18] Q. Wu, Y. Sun, H. Bai, G. Shi, *Phys. Chem. Chem. Phys.* **2011**, *13*, 11193.
- [19] a) Q. Guo, X. Zhou, X. Li, S. Chen, A. Seema, A. Greiner, H. Hou, *J. Mater. Chem.* **2009**, *19*, 2810; b) T. Bordjiba, M. Mohamedi, L. H. Dao, *Adv. Mater.* **2008**, *20*, 815.
- [20] M. Brandbyge, J.-L. Mozos, P. Ordejón, J. Taylor, K. Stokbro, *Phys. Rev. B* **2002**, *65*, 165401.
- [21] J. Xia, F. Chen, J. Li, N. Tao, *Nat. Nanotechnol.* **2009**, *4*, 505.
- [22] X. Blase, L. X. Benedict, E. L. Shirley, S. G. Louie, *Phys. Rev. Lett.* **1994**, *72*, 1878.
- [23] a) C. Ma, Z. Xiao, A. A. Puzos, A. P. Baddorf, W. Lu, K. Hong, J. Bernholc, A.-P. Li, *Phys. Rev. Mater.* **2018**, *2*, 014006; b) A. Ambrosi, C. K. Chua, A. Bonanni, M. Pumera, *Chem. Rev.* **2014**, *114*, 7150; c) C.-Y. Su, A.-Y. Lu, Y. Xu, F.-R. Chen, A. N. Khlobystov, L.-J. Li, *ACS Nano* **2011**, *5*, 2332.
- [24] a) T. Menanteau, M. Dias, E. Levillain, A. J. Downard, T. Breton, J. Phys. Chem. C **2016**, *120*, 4423; b) S. S. C. Yu, E. S. Q. Tan, R. T. Jane, A. J. Downard, *Langmuir* **2007**, *23*, 11074; c) A. K. Farquhar, H. M. Dykstra, M. R. Waterland, A. J. Downard, P. A. Brooksby, *J. Phys. Chem. C* **2016**, *120*, 7543.
- [25] a) S. Donner, H. W. Li, E. S. Yeung, M. D. Porter, *Anal. Chem.* **2006**, *78*, 2816; b) H. Tian, A. J. Bergren, R. L. McCreery, *Appl. Spectrosc.* **2007**, *61*, 1246.
- [26] K. H. Koch, K. Müllen, *Chem. Ber.* **1991**, *124*, 2091.
- [27] a) V. L. J. Joly, M. Kiguchi, S.-J. Hao, K. Takai, T. Enoki, R. Sumii, K. Amemiya, H. Muramatsu, T. Hayashi, Y. A. Kim, M. Endo, J. Campos-Delgado, F. López-Urías, A. Botello-Méndez, H. Terrones, M. Terrones, M. S. Dresselhaus, *Phys. Rev. B* **2010**, *81*, 245428; b) A. Reina, X. Jia, J. Ho, D. Nezich, H. Son, V. Bulovic, M. S. Dresselhaus, J. Kong, *Nano Lett.* **2008**, *9*, 30; c) R. L. McCreery, *Chem. Rev.* **2008**, *108*, 2646; d) Y. Wang, D. C. Alsmeyer, R. L. McCreery, *Chem. Mater.* **1990**, *2*, 557.
- [28] M. Supur, S. R. Smith, R. L. McCreery, *Anal. Chem.* **2017**, *89*, 6463.
- [29] J. Cai, P. Ruffieux, R. Jaafar, M. Bieri, T. Braun, S. Blankenburg, M. Muoth, A. P. Seitsonen, M. Saleh, X. Feng, K. Mullen, R. Fasel, *Nature* **2010**, *466*, 470.
- [30] W. Yang, A. Lucotti, M. Tommasini, W. A. Chalifoux, *J. Am. Chem. Soc.* **2016**, *138*, 9137.
- [31] Y. Gogotsi, P. Simon, *Science* **2011**, *334*, 917.
- [32] a) V. Augustyn, J. Come, M. A. Lowe, J. W. Kim, P.-L. Taberna, S. H. Tolbert, H. D. Abruña, P. Simon, B. Dunn, *Nat. Mater.* **2013**, *12*, 518; b) P. Simon, Y. Gogotsi, B. Dunn, *Science* **2014**, *343*, 1210.
- [33] S. Ranganathan, R. L. McCreery, S. M. Majji, M. Madou, *J. Electrochem. Soc.* **2000**, *147*, 277.
- [34] J. D. Ramsey, S. Ranganathan, J. Zhao, R. L. McCreery, *Appl. Spectrosc.* **2001**, *55*, 767.